Thermal Management of Large-Format Prismatic Lithium-Ion Battery in PHEV Application

View the article online for updates and enhancements.

Thermal Management of Large-Format Prismatic Lithium-Ion Battery in PHEV Application

Henrik Lundgren,[a,z] **Pontus Svens,**[b] **Henrik Ekström,**[a] **Carl Tengstedt,**[b] **Johan Lindström,**[b] **Mårten Behm,**[a,*] **and Göran Lindbergh**[a]

[a]*Applied Electrochemistry, Department of Chemical Engineering and Technology, KTH Royal Institute of Technology, SE-100 44 Stockholm, Sweden*
[b]*Scania CV AB, SE-151 87 Södertälje, Sweden*

Thermal effects are linked to all main barriers to the widespread commercialization of lithium-ion battery powered vehicles. This paper presents a coupled 2D electrochemical – 3D thermal model of a large-format prismatic lithium-ion battery, including a thermal management system with a heat sink connected to the surface opposite the terminals, undergoing the dynamic current behavior of a plug-in hybrid electric (PHEV) vehicle using a load cycle with a maximum current of 8 C, validated using potential and temperature data. The model fits the data well, with small deviations at the most demanding parts of the cycle. The maximum temperature increase and temperature difference of the jellyroll is found to be 9.7°C and 3.6°C, respectively. The electrolyte is found to limit the performance during the high-current pulses, as the concentration reaches extreme values, leading to a very uneven current distribution. Two other thermal management strategies, short side and long side surfaces cooling, are evaluated but are found to have only minor effects on the temperature of the jellyroll, with maximum jellyroll temperatures increases of 9.4°C and 8.1°C, respectively, and maximum temperature differences of 3.7°C and 5.0°C, respectively.
© 2015 The Electrochemical Society. [DOI: 10.1149/2.09411602jes] All rights reserved.

Temperature is one of the most important parameters for the performance, safety, and aging of lithium-ion batteries (LIBs), and good control of the battery temperature is crucial when designing a battery pack or module and its thermal management system. In fact, Bandhauer et al. point out that all the main barriers to the deployment of large LIB powered vehicle fleets: safety; cost (related to lifetime); and low-temperature performance, are linked to thermal effects in the battery, highlighting its importance.[1] With the introduction of large-format batteries, these issues become even more important.

Since the initial work by Bernardi et al.,[2] who developed a general energy balance for battery systems, several thermal models have been developed to study temperature effects in LIBs.[3–20] Most studies are limited to the case with constant current charge/discharge using moderate to low currents ($\leq$2C). However, there exists studies of more demanding cases such as White and Guo,[18] and Nieto et al.,[17] both studying high-current discharge (5C); and Zavalis et al., and Mao et al. studying short-circuit or near short-circuit conditions.[15,19] Furthermore, a few thermal models have been used to study temperature effects during dynamic cycling present in hybrid electric vehicle (HEV) or plug-in hybrid electric (PHEV) vehicle applications.[20–23] However, as stated by Bandhauer et al., in the majority of the studies "the performance of the battery or cell is not adequately characterized".[20]

Thermal management of lithium-ion batteries can be achieved either by using air as a cooling medium, a liquid (either flowing in a heat sink or surrounding the battery/module/pack), or a phase change material,[24,25] with the two former being the most common. For large-format batteries, only a liquid thermal management medium will provide good enough heat dissipation.[26] Several studies have included thermal management strategies into their thermal models.[12,14,16,18,20,27] However, with the exception of Bandhauer et al., few have compared different strategies,[20] other than comparing different cooling media, such as air and liquid or phase change material, using the same thermal management system. Bandhauer et al. uses a fully coupled 2D electrochemical-thermal model of a cross-section of an entire battery to study two different thermal management strategies: one strategy with the cooling medium surrounding the battery cells in the battery pack and one with internal cooling of the batteries.[20]

This study builds upon the work of Bandhauer et al. but expands it to include a very detailed 3D thermal model, but simplifies the electrochemical model to 2D geometry with the thickness of one cell-layer. The model is used to study thermal management cases more realistic to the vehicle industry: by placing the cells on a heat sink. The model is employed on a large-format 25 Ah prismatic cell in a PHEV application, emulated using a cycling scheme based on the ISO dynamic discharge power profile cycles A & B, but changed slightly and converted to current basis,[28] using the electrochemical model developed by Fuller, Doyle, and Newman.[29–31] Experimental data of cell potential and surface temperatures are used to validate the model of a base case with cooling through a heat sink connected to the surface opposite to the cell terminals. The model is then used to study other thermal management strategies, namely heat sinks connected to both of the short side surfaces or both of the long side surfaces, and also to investigate what limits the electrochemical and thermal performance of the cell.

Model Description

The model was set up using Comsol Multiphysics 5.0, with the physics interfaces "Lithium-Ion Battery" solving the electrochemical problem using a one-layer slice of the jellyroll, "Electric Currents" calculating the joule-heating of the terminals/current collectors, and "Heat Transfer in Solids" solving the thermal problem. The two models were coupled. The thermal model feeding the electrochemical model with the average temperature of the 3D jellyroll domain, and the electrochemical model returning a heat generation rate to the thermal model, which is averaged for the entire jellyroll. This means that only two variables are exchanged between the two models: the average temperature of the jellyroll from the thermal model to the electrochemical model, and the heat generation rate from the electrochemical model to the thermal model.

Using an electrochemical model with a lower dimension than the thermal model, with the temperature uniformly set to the average of the thermal model, significantly decreases the computational cost and memory usage. Crucial for the validity of this simplification is that the internal maximum temperature differences (ΔT) within the active battery material are low, and that the coupling between inhomogeneities in temperature and local current densities (and the resulting local heat production) for the resulting ΔT is fairly weak.

That simplification can be justified from earlier studies in literature using fully coupled models,[20,32,33] although cell chemistries, battery load profile, geometries and cooling strategies may vary compared to this study. For the investigated load cycle in this study the average C rate is about 1.7 C during the length of approximately 14 minutes, and the longest current pulse duration is a 5C discharge pulse with a duration of two minutes. The highest temperatures is expected to occur either at the end of the simulation or shortly after the 5C pulse.

Pannala et al.[33] have reported internal temperature differences for a complete 5C discharge for various geometries and cooling strategies using both "loosely" coupled (similar to the coupling approach used in this study) and "tightly" coupled models (with spatially resolved temperature dependent electrochemistry). The highest ΔT found was 15°C for a battery with a thickness comparable ours, but for a quite extreme cooling case with liquid cooling along the long sides of a pouch battery. For our 1.7 C average load cycle this result would still translate to a ΔT of only a few degrees at the end of the cycle, assuming a crude $R \cdot I^2$ conversion of the generated heat, and also considering that heat dissipation typically increases with higher temperatures. Lee et al.[33] reported temperature distributions for fully coupled electrochemical-thermal modeling work on cylindrical batteries. The ΔT's were highly dependent on the number of tabs. For 20 Ah cells with 10 tabs or more, which would correspond to our battery configuration, steady-state ΔT's of 8.3°C were achieved after 90 min of continuous cycling above 5C. Also this result scales down to a ΔT in the range of 1°C using a $R \cdot I^2$ conversion of the generated power. With regard to pulse responses, Lee reported a ΔT of less than 3°C after a 5 min 4C discharge pulse. Bandhauer et al.[20] report ΔT's in the range of a few degrees for a prismatic 20 Ah battery when using a battery load cycle similar to the one used in this study. These results support our assumption that the ΔT's in this study should be expected to be in the range of a few degrees.

The coupling between between inhomogeneities in temperature and local current densities was investigated by Pannala et al.[32] who found "very little differences between the coupling strategies indicating the feedback between the electrochemical and thermal processes is weak". For currents up to 3C a spatially resolved temperature coupling had small (less than 1%) effects on the average heat source on the battery. Typically a tighter coupling renders slightly lower heat sources due to reduced internal resistances at higher temperatures. It should be noted however that temperature effects on the solid state diffusion of solid lithium was not included in the study of Pannala et al.[32]

Electrochemical model.— The 2D geometry used for the electrochemical model can be seen in Figure 1, also including a colormap of the used materials in the Comsol Multiphysics materials library for the different model domains. The rectangular geometry is a simplified representation of the actual geometry in the studied battery cell, which consisted of several layers rolled in a jellyroll. The model geometry is a one cell layer thick plane from the positive terminal/current collector to negative terminal/current collector.

For the domains containing electrolyte, i.e. the two electrodes and the separator, the governing equations are the conservation of current and a mass balance for the salt, using concentrated electrolyte theory:

$$i_{tot} = \varepsilon_L^\beta \nabla \cdot \left(-\sigma_L \nabla \Phi_L + \frac{2\sigma_L RT}{F} \left(1 + \frac{\partial ln f_\pm}{\partial ln c_L} \right) (1 - t_+) \nabla ln c_L \right) \quad [1]$$
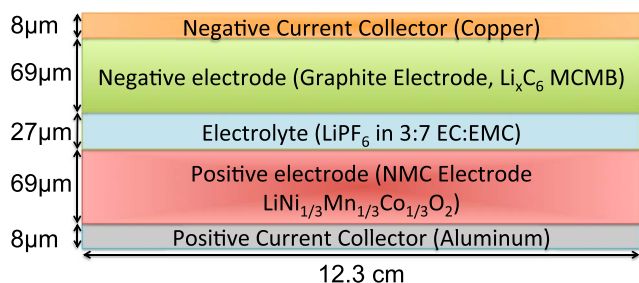

Figure 1. Geometry and material color map for the electrochemical model. Note that only half of the thickness of the current collectors is included in the model (The full thickness is 16 μm), as they are coated on both sides.

$$\varepsilon_L \frac{\partial c_L}{\partial t} + \varepsilon_L^\beta \nabla \cdot (-D_L \nabla c_L) = \frac{-i_{tot}}{F} t_+ \quad [2]$$

$$D_L = \tilde{D}_L \left(1 + \frac{\partial ln f_\pm}{\partial ln c_L} \right) \frac{c_{tot}}{c_{solv}} \left(1 - c_L V_m^{LiPF_6} \right) \quad [3]$$

$$c_{solv} = \frac{\left(1 - V_m^{LiPF_6} \right) c_L}{V_m^{solv}} \quad [4]$$

where i is the current density, i_{tot} (A m^{-3}) the electrochemical reaction current source, σ_L the electrolyte ionic conductivity, Φ_L the electrolyte potential, R the universal gas constant (8.314 J K^{-1}mol^{-1}), T the temperature, F the Faraday constant (96485 C mol^{-1}), $1 + \partial ln f_\pm / \partial ln c_L$ the thermodynamic enhancement factor, t_+ the cationic transport number, c_L the electrolyte salt concentration, ε_L the electrolyte volume fraction, β the Bruggeman coefficient, D_L the apparent salt diffusion coefficient, and $\tilde{D}_L$ the salt diffusion coefficient with respect to the thermodynamic driving force.

For the porous electrodes, the domain equations are conservation of current along with a mass balance over the electrode particles, according to the following equations:

$$i_S = -\sigma_S \nabla \Phi_S \quad [5]$$

$$\nabla \cdot i_S = -i_{tot} \quad [6]$$

$$i_{tot} = A i_{loc} \quad [7]$$

$$\frac{\partial c_S}{\partial t} = \nabla \cdot (D_S \nabla c_S) \quad [8]$$

$$SOC = \frac{c_S}{c_{S,max}} \quad [9]$$

Boundary conditions:

$$\text{At } z_{Neg} = 0 : \frac{\partial c_S}{\partial z} = 0, \text{ at } r_{Pos} = 0 : \frac{\partial c_S}{\partial r} = 0 \quad [10]$$

$$\text{At } z_{Neg} = r_{p,Neg} : -D_{S,Neg} \frac{\partial c_S}{\partial z} = \frac{i_{loc}}{F}, \text{ at } r_{Pos}$$

$$= r_{p,Pos} : -D_{S,Pos} \frac{\partial c_S}{\partial r} = \frac{i_{loc}}{F} \quad [11]$$

where the gradient is solved using Cartesian coordinates for the negative electrode (assuming flake shaped particles, i.e. thin, flat layers) and spherical coordinates for the positive electrode (assuming spherical particles), see Eqs. 10 and 11, and where σ_S is the electrical conductivity, Φ_S the electric potential, D_S the solid state diffusion coefficient, A the specific area of the electrode particles, and c_S the lithium concentration in the solid phase. For the charge transfer kinetics, the Butler-Volmer equation is used:

$$i_{loc} = i_{0,i} \left(exp \left(\frac{\alpha_{a,i} F \eta}{RT} \right) - exp \left(\frac{-\alpha_{c,i} F \eta}{RT} \right) \right) \quad [12]$$

$$i_{0,i} = F \left(\frac{i_{0,i,max}}{F c_{s,i,max}} \right)^{\alpha_{a,i} + \alpha_{c,i}} \left(c_{s,i,max} - c_s \right)^{\alpha_{a,i}} c_s^{\alpha_{c,i}} \left(\frac{c_L}{c_{L,0}} \right)^{\alpha_{a,i}} \quad [13]$$

where i_0 is the exchange current density, η the overpotential, and α the electrochemical reaction symmetry factor. The ionic conductivity, thermodynamic enhancement factor, electrolyte salt diffusion coefficient, and the solid state diffusion coefficient for the negative electrode are assumed to be functions of temperature using an Arrhenius expression:

$$n(T) = n(T_{ref}) \cdot exp \left(\left(\frac{E_a}{R} \right) \left(\frac{1}{T_{ref}} - \frac{1}{T} \right) \right) \quad [14]$$

where T_{ref} is a reference temperature at which the property n is known, and E_a the activation energy for the temperature dependence. The electrochemical model is considered to be isothermal at every time step and is evaluated at the average jellyroll temperature from the thermal model. Even though the model is isothermal, a 2D geometry was chosen since our initial assumption was that potential drops in the long
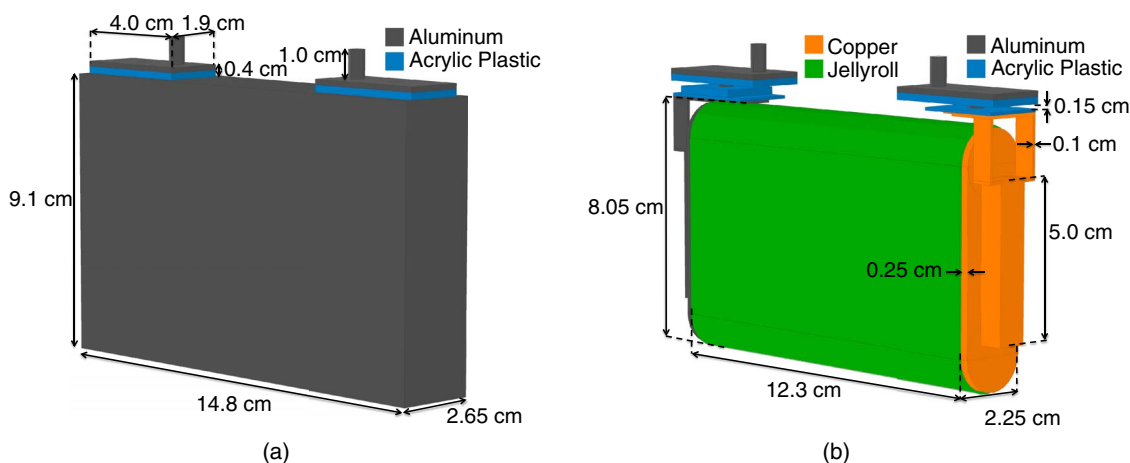
Figure 2. Outer and inner geometry and material color map for the thermal model of the studied battery cell following the geometric design standard DIN SPEC 91252:2011-01.[41]

metal foil current collectors might lead to uneven current distribution. Property values/expressions for the electrochemical model are listed in Table I.

Thermal model.— The Comsol Multiphysics physics interface "Heat Transfer in Solids" used in this study solves a thermal energy balance over the entire geometry, neglecting all modes of heat transfer except conduction, see Eq. 15.[1,9,13,15]

$$\rho C_p \frac{\partial T}{\partial t} = \nabla \left(k \nabla T \right) + Q \qquad [15]$$

where ρ is the density, C_p the heat capacity at constant pressure, k the thermal conductivity, and Q the heat generation rate, which is zero for all domains except the jellyroll, the current collectors, and the terminals. The heat generation rate for the jellyroll is calculated from the electrochemical model according to Eq. 16 and distributed uniformly into the entire volume of the jellyroll.

$$Q_{Jellyroll} = \frac{\int_{Battery} \left(i_{tot} \left(\overbrace{\Phi_S - \Phi_L - E_{Eq}}^{\eta} \right) + i_{tot} \left(T \frac{\partial E_{Eq}}{\partial T} \right) - \left(\boldsymbol{i_S} \cdot \nabla \Phi_S + \boldsymbol{i_L} \cdot \nabla \Phi_L \right) \right) d\Omega}{\int_{Battery} d\Omega} \qquad [16]$$

where η is the overpotential, E_{Eq} the equilibrium potential, and $d\Omega$ a volume element in the battery, and where the first term on the right hand side is the irreverisble heat generation, the second term the reversible heat generation (entropic heat), and the third therm the Joule heating. The equilibrium potential curves were taken from Srinivasan and Newman for the negative electrode,[38] and from Zheng et al. for the positive electrode.[36] The values for $\partial E_{Eq}/\partial T$ were taken from Thomas and Newman,[39] and Viswanathan et al.,[40] for the negative and positive electrode respectively. For the current collectors/terminals (all aluminum and copper parts in Figure 3b) heat is generated by Joule heating calculated using the physics interface "Electric Currents":

$$Q_{Joule} = -\boldsymbol{i_S} \cdot \nabla \Phi_S \qquad [17]$$

The simulated potential is calculated as the combination of the potential from the electrochemical model and the over-potentials of the current collectors.

The model geometry can be seen in Figure 2, also including colormap of the materials used in the Comsol Multiphysics materials library, with the void space not shown is assumed to be filled with argon, and a table of the material properties in Tables II and III.

All boundaries were considered to be thermally insulated, $k\nabla T = 0$, except the surface connected to the heat sink, which was kept at a constant temperature of T = 20°C. An 80 μm thick thermally resistive film was assumed between the heat sink and the battery, and a 350 μm thick film between the jellyroll and the cell can, with the thermal properties of acrylic plastic to serve as a thermal contact resistance and insulation (present in the commercial battery), respectively.

Experimental

The studied battery was a prismatic cell from a well-known supplier following the geometric design standard DIN SPEC 91252:2011-01.[41] The cell was previously unused and had a capacity of 25 Ah and rated to a maximum current of 200 A (8 C). Internal geometry was determined by cell disassembly, and electrode composition by energy dispersive X-ray spectroscopy (EDX) using a X-max 50 detector from Oxford instruments. Particle sizes were measured using a Zeiss Sigma VP Field-Emission Scanning Electron Microscope (FE-SEM) with an In-lens secondary electron detector and using accelerator voltages of 1–3 kV.

The electrochemical cycling was performed using a PEC SBT0550. The cycling scheme was based on the ISO dynamic discharge power profile cycles[28] (One cycle A followed by one cycle B), but was converted from power basis to current basis, see Figure 3, and changed slightly. The changes were at the current step starting at 176 s in each cycle (corresponding to 176 s and 536 s in Figure 4), from 1 C charge to discharge. This yields a total SOC difference of −34.2%.

The battery cell was mounted on a heat sink that was temperature controlled using a Lauda XT550 process thermostat and then placed inside an Espec BPU-3 temperature chamber to ensure uniform initial temperature distribution. The battery was covered in several layers of plastic foam, to create near-adiabatic conditions at all boundaries except the surface connected to the heat sink. 6 type K thermocouples were connected to the cell, as seen in Figure 4 also showing the definition of the surface opposite to the terminals that is cooled in the base case, along with long and short side surfaces used for the thermal management strategy comparisons. The thermocouples were

Table I. Electrochemical model properties.

Property	Value / unit	E_a / kJ mol^{-1}	T_{ref} / K	Reference
σ_L	$1.297c_L^3 - 25.1c_L^{1.5} + 33.29c_L$ / mS cm^{-1}	4000	298	15,37
$1 + \frac{\partial ln f_{\pm}}{\partial ln c_L}$	$\frac{0.28687c_L^2 - 0.74678c_L + 0.44103}{0.1287c_L^3 - 0.4106c_L^2 + 0.4717c_L + 0.5508}$ / -	-1000	298	15,37
t_+	$-0.1287c_L^3 + 0.4106c_L^2 - 0.4717c_L + 0.4492$ / -	-	-	37
$\tilde{D}_L$	$8.794 \cdot 10^{-11}c_L^2 - 3.792 \cdot 10^{-10}c_L + 4.862 \cdot 10^{-10}$ / m^2 s^{-1}	16500	298	15,37
$V_m^{LiPF_6}$	$59 \cdot 10^{-3}$ / dm^3 mol^{-1}	-	-	37
V_m^{solv}	$87 \cdot 10^{-3}$ / dm^3 mol^{-1}	-	-	37
$\varepsilon_{L,Neg}$	0.31 / -	-	-	34
$\varepsilon_{L,Pos}$	0.29 / -	-	-	34
$\varepsilon_{L,Sep}$	0.4 / -	-	-	15
β	2.1 / -	-	-	Estimated
$\sigma_{S,Neg}$	100 / S m^{-1}	-	-	13
$\sigma_{S,Pos}$	91 / S m^{-1}	-	-	36
$\sigma_{S,Neg\ CC}$	$5.998 \cdot 10^7$ / S m^{-1}	-	-	35
$\sigma_{S,Pos\ CC}$	$3.77 \cdot 10^7$ / S m^{-1}	-	-	35
$c_{S,max,Neg}$	31.858 / mol dm^{-3}	-	-	13
$c_{S,max,Pos}$	29.000 / mol dm^{-3}	-	-	Estimated
$D_{S,Neg}$	$1.4523 \cdot 10^{-13}$ / m^2 s^{-1}	68025.7	318	13
$D_{S,Pos}$	$5 \cdot 10^{-13}$ / m^2 s^{-1}	-	-	36
$r_{p,Neg}$	49.3 / nm	-	-	Measured
$r_{p,Pos}$	255.2 / nm	-	-	Measured
$\varepsilon_{S,Neg}$	0.62 / -	-	-	15
$\varepsilon_{S,Pos}$	0.482 / -	-	-	15
$\alpha_{a,Neg}$	0.5 / -	-	-	Assumed
$\alpha_{c,Neg}$	0.5 / -	-	-	Assumed
$\alpha_{a,Pos}$	0.5 / -	-	-	Assumed
$\alpha_{c,Pos}$	0.5 / -	-	-	Assumed
$i_{0,Neg,max}$	0.5 / A m^{-2}	-	-	Estimated from 15
$i_{0,Pos,max}$	1.5 / A m^{-2}	-	-	Estimated from 15
SOC_0	0.755 / -	-	-	Estimated
$c_{L,0}$	1.0 / mol dm^{-3}	-	-	Assumed

Table II. Thermal model material properties.

Material	ρ / kg m^{-3}	C_p / J kg^{-1}K^{-1}	k / W m^{-1}K^{-1}	Reference
Aluminum	2700	900	238	35
Copper	8700	385	400	35
Acrylic plastic	1190	1470	0.18	35
Argon	$522.2077T^{-1}$	520.3264	$-2.420719 \cdot 10^{-4}$ $+7.233846 \cdot 10^{-5}T^1$ $-5.020862 \cdot 10^{-8}T^2$ $+2.864443 \cdot 10^{-11}T^3$	35
Jellyroll	2560	975	Table III	Calculated from 15, in accordance with 42

electrically insulated using a thin plastic film to avoid interference form the aluminum cell case, and then attached to the cell using highly thermally conductive copper tape. Virtual probes were placed at the same locations in Comsol Multiphysics.

Table III. Thermal conductivity for the jellyroll. To reduce geometry complexity, the jelly-roll is homogenized with an anisotropic thermal conductivity,[40] here given in the in-plane and through-plane directions. For the rectangular block part of the jelly roll, the in-plane direction corresponds to the *x* / *z*-directions, and the through-plane direction to the *y*-direction. A cylindrical coordinate system transformation was used do define the anisotropic conductivity in the half cylinders forming the top and bottom of the jellyroll.

$k_{through-plane}$ / W m^{-1}K^{-1}	$k_{in-plane}$ / W m^{-1}K^{-1}
0.95	30.8

Results and Discussion

The particle sizes used in the electrochemical model were measured using SEM, see Figure 5. Both electrodes consisted of agglomerates with a radius of about 5 μm, consisting of smaller particles used in the electrochemical model. For the positive electrode, the average radius of the particles were 252.2 nm ± 36.3 nm, and for the negative electrode the average thickness of the graphite layers were 49.3 nm ± 9.9 nm. EDX measurements showed that the positive electrode consisted of $Ni_{1/3}Mn_{1/3}Co_{1/3}O_2$ and the negative electrode of mostly carbon. However, the exact compositions of the electrodes are unknown, as the studied battery is a commercial cell with no supplier information.

The results from the electrochemical and thermal modeling have been divided into two subsections: One with the base case with cooling on the surface opposite to the terminals, which is the way the cells will be cooled in the intended vehicle and for which experiments to validate the model was performed; and one with a comparison of the
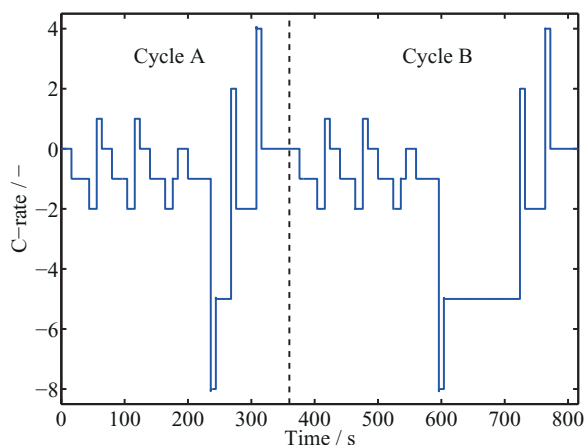
Figure 3. Used cycling scheme, based on the ISO dynamic discharge power profiles. The used cycling scheme starts with one cycle A, followed by one cycle B, (i.e. A→B).

cases with cooling on both of the short sides or both of the long sides. Cooling is implemented in all cases by connecting the appropriate surface to a heat sink with a constant temperature of 20°C, with a thermal contact resistance equivalent to 80 μm of acrylic plastic.

Base case – Cooling opposite the terminals.— A comparison of experimental and simulated cell voltage as functions of time can be seen in Figure 6. The model fit is good, with a maximum error of 38 mV at the end of the 8 C discharge ending at 604 s, indicating that the model will accurately determine the irreversible heat generation rate for the thermal model. A possible cause to the deviations of the potential curves is a mismatch in the equilibrium potential between the model and the experiments, and will thus not affect the heat generation rate.

Figure 7 displays experimental and modeled surface temperatures at different locations on the battery, where T1 and T2 correspond to the negative and positive terminal, respectively, and T3 to T6 correspond to different places on the long side. The exact locations of these probes can be found in Figure 4. The model fit is fair, with good agreement between the model and experimental results for the probes on the long side, but starts to deviate slightly during the long 5 C discharge pulse ending at 724 s, with a maximum error of about 2°C. It is apparent that
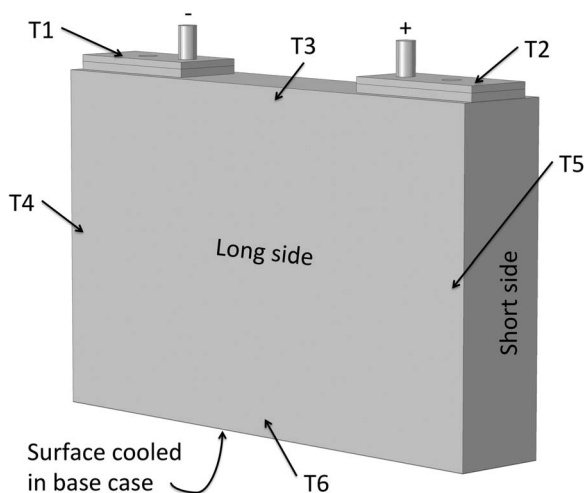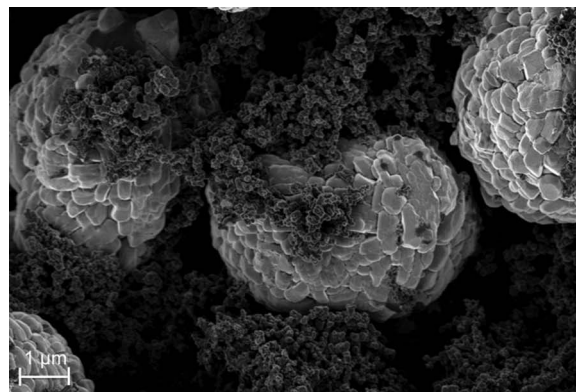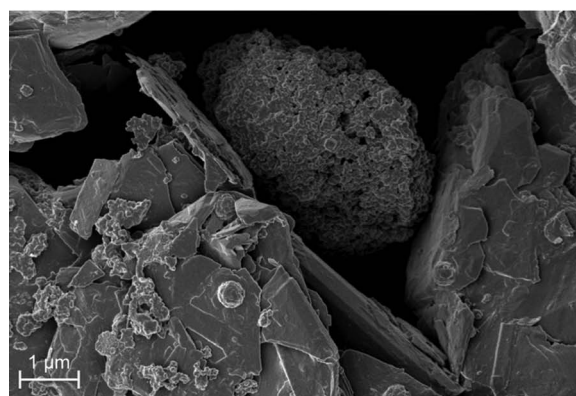

(a)

(b)

Figure 5. SEM images of a) the positive NMC electrode, and b) the negative graphite electrode. An in-lens secondary electron detector and an accelerator voltage of 1 kV was used for both images.

the model does not capture the process responsible for the temperature peaks at the terminals after the high current peaks. This is believed to be due to electrical contact resistances between the cables and the terminals, and also due to the fact that the cables themselves possibly serve as heat sources (during high current discharge) and heat sinks (during open circuit) during these experiments, features which were not included in the model. The reason why T1 and T2 is underestimated at the same time as T3 is overestimated is unclear, but is an effect of that the experimental setup is not fully captured in the thermal model. To improve the fit of the temperature probes, more
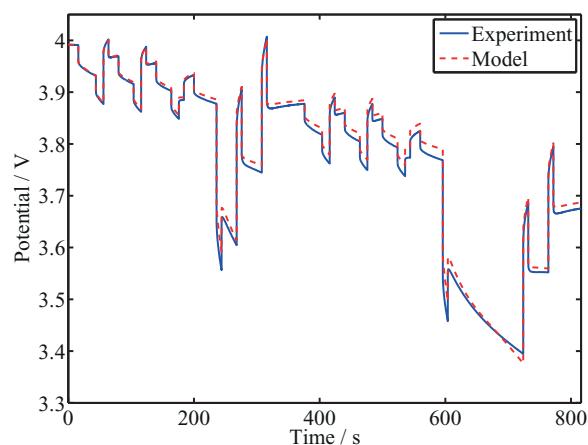

Figure 4. Schematic picture of the studied battery with the placement of the experimental temperature probes (T1-T6), and definition of the surface opposite to the terminals cooled in the base case, as well as long and short side surfaces.

Figure 6. Comparison of experimental and simulated cell voltages as functions of time.
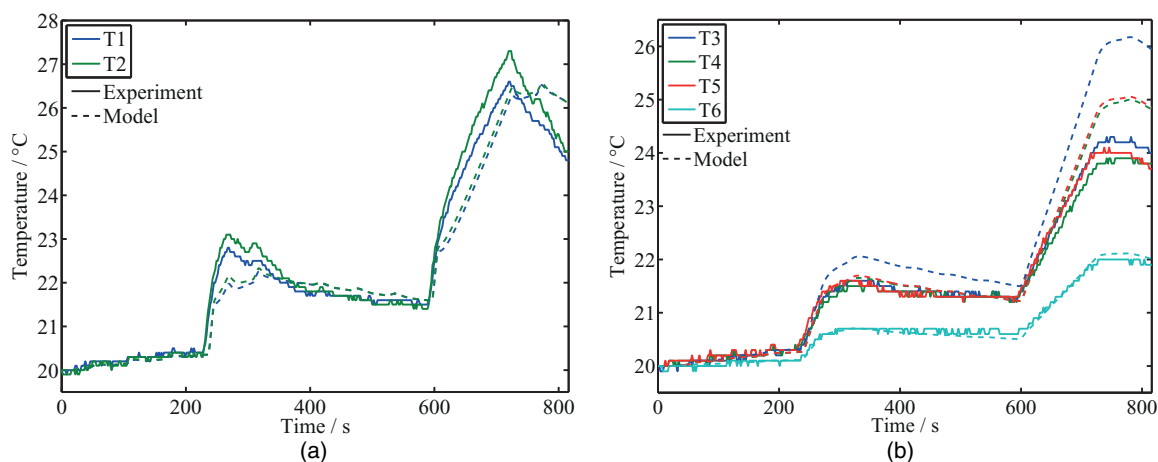
Figure 7. Comparison of experimental (solid lines) and simulated (dashed lines) a) terminal temperatures and b) long side surface temperatures as functions of time.

controlled thermal experiments should be performed, as well as better characterization of the input data for the electrochemical model, e.g. by investigating the temperature dependency of parameters such as the exchange current density etc.

Turning then to the inside of the battery, Figure 8a displays a snapshot of the temperature distribution inside the battery and the terminals at 724 s, i.e. at the end of the 120 s 5 C discharge pulse, and Figure 8b a graph of the maximum and minimum temperature in the jellyroll as functions of time. The jellyroll reaches a maximum of almost 30°C, and the largest temperature difference within the jellyroll is 3.6°C, which could have detrimental effects in the long perspective. It becomes clear that the contact between the jellyroll and the cell can is extremely important for the thermal performance of the battery, and in fact most of the heat is dissipated through the long side of the battery. To investigate the main path of heat transport inside the battery, the integrated heat flux over the jellyroll boundaries was compared for different times in the simulation results. Generally the bulk of the heat was conducted through the long sides of the jellyroll. On average over the whole cycle less than about 10% of the heat generated inside the jellyroll was dissipated through the current collectors. Some temporal variations in this figure were however seen, with a maximum of about 50% at the very beginning of the 8 C current pulses. Not surprisingly, most of the heat is being generated in the jellyroll, with only about 5% of the total heat being generated in the current collectors/terminals. The heat flux streamlines from the jellyroll to the bottom plate at time 724 s are plotted in Figure 8c. The streamlines represent the path of heat transfer for 300 evenly distributed points on the jellyroll surface.

Simulations were done where the contact between the jellyroll and the cell can be removed, which resulted in most of the produced heat being accumulated in the jellyroll, showing that the current collectors/terminals are not capable of dissipating the amount of heat that is being generated during high power operation. As the battery ages, the contact between the jellyroll and the cell can will change, either increasing the contact due to jellyroll swelling or losing contact due to gas generation, since the internal pressure increases with aging.[43,44]

Looking inside the jellyroll, the hottest parts are found in the center of the jellyroll (Figure 9). This uneven temperature distribution will result in highly uneven aging over time, and can probably explain the aging behavior observed by Klett et al.,[45] with more aging in the core of the jellyroll.

To investigate the validity of using a 2D electrochemical battery cell model of uniform temperature, a simulation running two battery models connected in parallel was performed, subjected to the currents of the load cycle multiplied by two. One battery was set uniformly to a constant temperature of 23°C and the other one to 27°C in this simulation. The peak currents and generated heat between the two batteries differed less than 2%, in line with the results reported by Pannala et al.[32] discussed above. From this it can be concluded that using a fully distributed 3D electrochemical model of non-uniform temperature in the jellyroll would have little impact on the results of this study. As a way to link the performance to the electrochemical processes, the local current densities and electrolyte concentration were studied. No variations in any parameters along the length of the jellyroll for the electrochemical model with uniform temperature
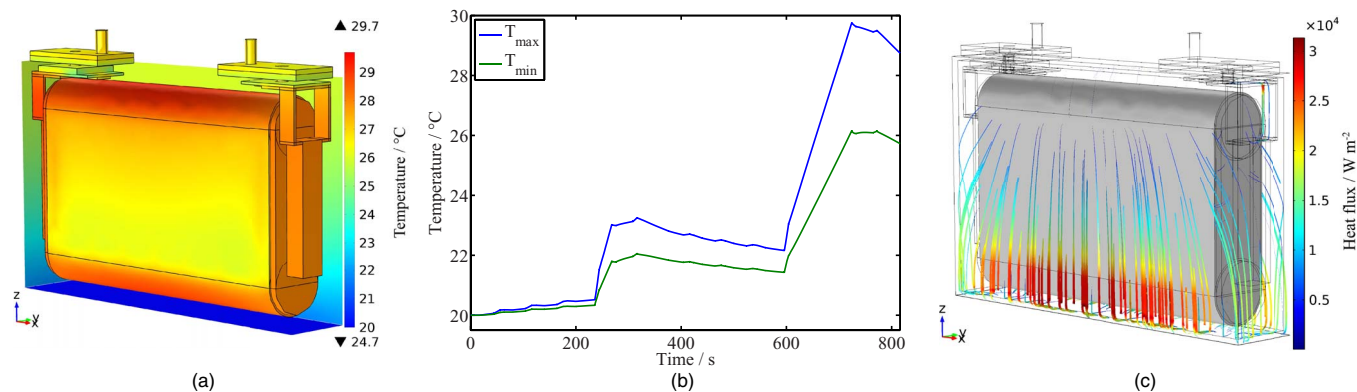

Figure 8. Modeled temperature distributions of the battery for a) 3D snapshot at 724 s for jellyroll, terminals, and three cell can surfaces; b) maximum and minimum temperature in the jellyroll as functions of time; and c) heat flux streamlines originating from the jellyroll surface. The heat flux magnitude (Euclidian norm) is depicted by the width and color of the streamlines.
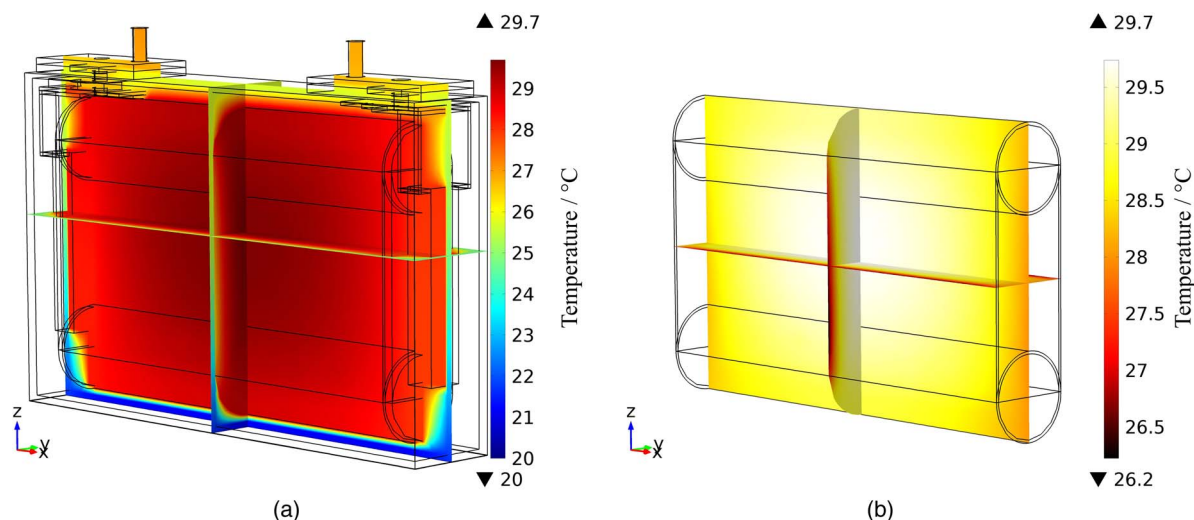
Figure 9. Cross section of temperature distribution at 724 s for a) entire battery cell b) jellyroll. Note the different temperature scales.

used in this study were observed, i.e. nothing was gained from using a 2D geometry, and all results will therefore be presented as 1D. In Figure 10a it can be seen that most of the current is being produced at the parts of the electrodes close to the separator, with near zero current densities at the domains closest to the current collectors. This is likely connected to the fact that local electrolyte concentration (Figure 10b) reaches extreme values at these points, and large variations in local SOC (Figure 10c), varying from 15% to 70% at different locations in

the negative electrode at 724 s, and similarly between 45% and 80% for the positive electrode.

Alternative cooling strategies.— How to design your thermal management system is crucial for the thermal performance of a battery system. In this section, two alternative cooling strategies are evaluated using the thermal model: cooling the short side surfaces of the battery, and cooling the long side surfaces of the battery by using a heat
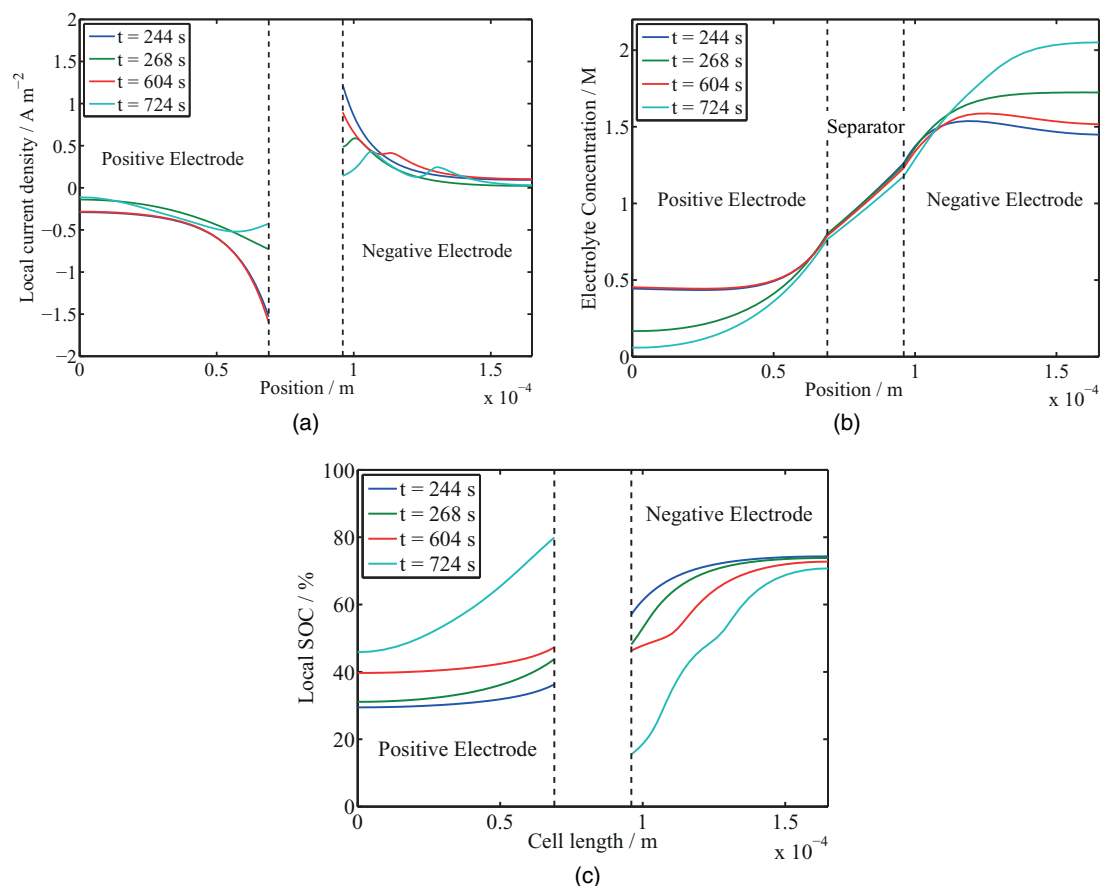

Figure 10. a) Local current density, b) Local electrolyte concentration and c) local SOC at selected times.
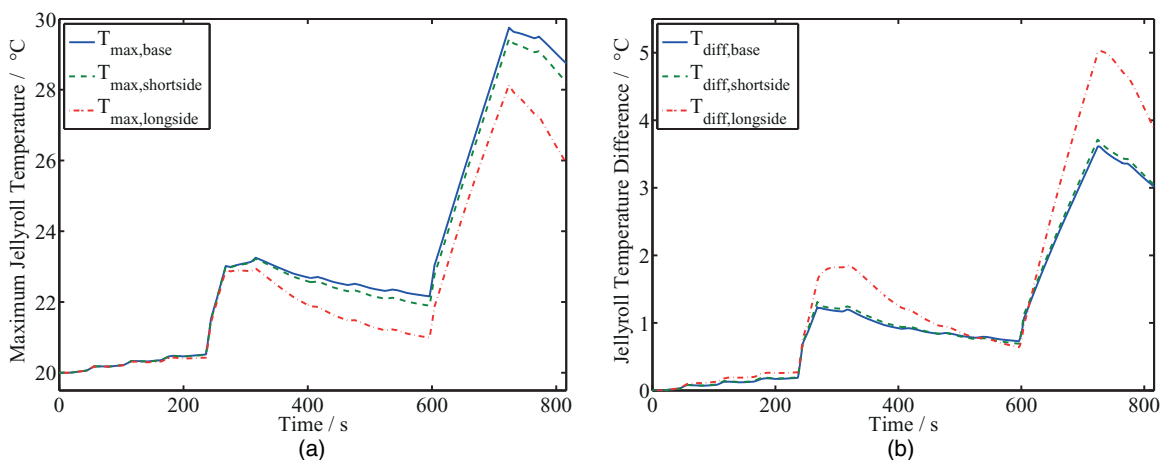
Figure 11. Three different cooling strategies: cooling the surface opposite to the terminals, cooling the short side surfaces, and cooling the long side surfaces evaluated by a) Maximum temperature of the jellyroll and b) temperature difference within the jellyroll, both as functions of time.

sink, as in the base case. Figure 11 displays the maximum jellyroll temperature, and temperature difference between the maximum and the minimum temperature of the jellyroll, both as functions of time.

It can be seen that all studied cooling strategies have similar thermal performance, with a maximum jellyroll temperatures of 29.7°C, 29.4°C, and 28.1°C for the base case, short side surfaces, and long side surfaces cooling, respectively. The temperature gradient within the jellyroll is not changed significantly for the short side cooling case, from 3.6°C for the base case to 3.7°C for short side cooling. However, for long side cooling case the gradient increases by almost 1.5°C to 5.0°C, because of the effective cooling of the parts of the jellyroll pressing to the cell can. The average jellyroll temperature difference (Figure 11b) is 0.93°C, 0.95°C, and 1.20°C for the base, short side, and long side cooling case, respectively. Clearly, the cell can is not the component limiting the thermal performance, instead the limitations lie in the heat transfer within the jellyroll. Depending on what metric, maximum temperature or temperature difference for the jellyroll, is considered to be least acceptable for the battery it is either the base case cooling strategy or the long side cooling strategy that performs the worst, with short side cooling being a good alternative, reducing the maximum temperature and while keeping the gradient relatively low.

Conclusions

The electrochemical and thermal performance of a commercial 25 Ah prismatic cell with graphite/NMC electrodes was characterized using a combined 2D electrochemical model coupled with a 3D thermal model validated against both cell potential and surface temperature measurements during an emulated PHEV cycle. The cycle consisted of slightly modified versions of ISO Dynamic Discharge Power Profile A & B converted to current basis. The model fits were found to be good, with a slight overestimation of the surface temperature after the most demanding pulses of the cycle. The maximum temperature during the cycle was ~27°C for the terminals, and between 22 and 24°C for different locations on the long side surfaces. The model predicts that the maximum temperature of the jellyroll during the cycle was 29.5°C, at which point there is a 3.5°C temperature difference between the hottest and coldest part of the jellyroll, a temperature difference that is expected to lead to uneven aging with the core of the jellyroll aging faster. The complex 3D geometry used gave some very useful insights to the thermal design of the battery, such as that most of the heat is dissipated through the cell can and not through the terminals, which would have been impossible if geometry of less complexity would have been used. The electrolyte is found to limit the performance during the high current pulses, with concentrations reaching extreme levels, leading to a very uneven current distribution

and leaving parts of the electrodes nearly unused. The model was also used to evaluate different cooling strategies, where the base case with a constant temperature (20°C) heat sink connected to the surface opposite the terminals was compared to cases where the heat sink was instead connected to the short side or long side surfaces. It was found that cooling strategies have similar performance. However, the case with cooling on the long sides showed some slightly different features, with a reduction of the maximum jellyroll temperature by more than 1.5°C, but an increase in the maximum jellyroll temperature difference by almost 1.5°C, which might make that strategy less beneficial than the base case.

List of Symbols

$1+\frac{\partial ln f_{\pm}}{\partial ln c_L}$	Thermodynamic enhancement factor
A	Specific area
c	Concentration
C_p	Heat capacity at constant pressure
D_L	Apparent diffusion coefficient
$\tilde{D}_L$	Diffusion coefficient with respect to thermodynamic driving force
E_a	Activation energy
F	Faraday's constant
i	Current density
i_0	Exchange current density
i_{tot}	Volumetric electrochemical current source
k	Thermal conductivity
Q	Heat generation rate
R	Ideal gas constant
t	Time
t_+	Transport number with respect to the solvent
T	Temperature
V_m	Partial molar voume

Greek

α	Electrochemical reaction symmetry factor
β	Bruggeman coefficient
ε	Volume fraction
η	Overpotential
ρ	Density

σ_L Ionic conductivity
σ_S Electronic conductivity
Φ Electric potential

Subscripts

L Electrolyte phase
S Solid phase

References

1. T. M. Bandhauer, S. Garimella, and T. F. Fuller, *J. Electrochem. Soc.*, **158**, R1 (2011).
2. D. Bernardi, E. Pawlikowski, and J. Newman, *J. Electrochem. Soc.*, **132**, 5 (1985).
3. Y. Chen and J. W. Evans, *J. Electrochem. Soc.*, **140**, 1833 (1993).
4. C. R. Pals and J. Newman, *J. Electrochem. Soc.*, **142**, 3274 (1995).
5. C. R. Pals and J. Newman, *J. Electrochem. Soc.*, **142**, 3282 (1995).
6. L. Rao and J. Newman, *J. Electrochem. Soc.*, **144**, 2697 (1997).
7. G. G. Botte, *J. Electrochem. Soc.*, **146**, 914 (1999).
8. L. Song and J. W. Evans, *J. Electrochem. Soc.*, **147**, 2086 (2000).
9. W. B. Gu and C. Wang, *J. Electrochem. Soc.*, **147**, 2910 (2000).
10. V. Srinivasan and C. Wang, *J. Electrochem. Soc.*, **150**, A98 (2003).
11. K. E. Thomas and J. Newman, *J. Electrochem. Soc.*, **150**, A176 (2003).
12. S.-C. Chen, Y.-Y. Wang, and C.-C. Wan, *J. Electrochem. Soc.*, **153**, A637 (2006).
13. K. Kumaresan, G. Sikha, and R. E. White, *J. Electrochem. Soc.*, **155**, A164 (2008).
14. M. Guo and R. E. White, *J. Electrochem. Soc.*, **158**, A1166 (2011).
15. T. G. Zavalis, M. Behm, and G. Lindbergh, *J. Electrochem. Soc.*, **159**, A848 (2012).
16. Y. Ye, Y. Shi, N. Cai, J. Lee, and X. He, *J. Power Sources*, **199**, 227 (2012).
17. N. Nieto, L. Diaz, J. Gastelurrutia, I. Alava, F. Blanco, J. Carlos Ramos, and a. Rivas, *J. Electrochem. Soc.*, **160**, A212 (2012).
18. M. Guo and R. E. White, *J. Power Sources*, **221**, 334 (2013).
19. J. Mao, W. Tiedemann, and J. Newman, *J. Power Sources*, **271**, 444 (2014).
20. T. M. Bandhauer, S. Garimella, and T. F. Fuller, *J. Electrochem. Soc.*, **162**, A125 (2015).
21. S. Allu, S. Kalnaus, W. Elwasif, S. Simunovic, J. a. Turner, and S. Pannala, *J. Power Sources*, **246**, 876 (2014).
22. G.-H. Kim, K. Smith, K.-J. Lee, S. Santhanagopalan, and A. Pesaran, *J. Electrochem. Soc.*, **158**, A955 (2011).
23. K. Smith and C.-Y. Wang, *J. Power Sources*, **160**, 662 (2006).
24. S. Al-Hallaj and J. R. Selman, *J. Power Sources*, **110**, 341 (2002).
25. R. Kizilel, R. Sabbah, J. R. Selman, and S. Al-Hallaj, *J. Power Sources*, **194**, 1105 (2009).
26. Z. Rao and S. Wang, *Renew. Sustain. Energy Rev.*, **15**, 4554 (2011).
27. U. S. Kim, J. Yi, C. B. Shin, T. Han, and S. Park, *J. Electrochem. Soc.*, **160**, A990 (2013).
28. Electrically Propelled Road Vehicles - Test Specifications for Lithium-Ion Traction Battery Packs and Systems - Part 2: High Energy Application, ISO 12405-2, 2010.
29. M. Doyle, T. F. Fuller, and J. Newman, *J. Electrochem. Soc.*, **140**, 1526 (1993).
30. T. F. Fuller, M. Doyle, and J. Newman, *J. Electrochem. Soc.*, **141**, 982 (1994).
31. T. F. Fuller, M. Doyle, and J. Newman, *J. Electrochem. Soc.*, **141**, 1 (1994).
32. S. Pannala, J. A. Turner, S. Allu, W. R. Elwasif, S. Kalnaus, S. Simunovic, A. Kumar, J. J. Billings, H. Wang, and J. Nanda, *J. Applied Physics*, **118**, 072017 (2015).
33. K. J. Lee, K. Smith, A. Pesaran, and G. H. Kim, *J. Power Sources*, **241**, 20 (2013).
34. S. Brown, N. Mellgren, M. Vynnycky, and G. Lindbergh, *J. Electrochem. Soc.*, **155**, A320 (2008).
35. Material property database (MPDB), JAHM Software, Inc.
36. W. Zheng, M. Shui, J. I. E. Shu, S. Gao, D. a N. Xu, L. Chen, L. I. N. Feng, and Y. Ren, *Bull. Mater. Sci.*, **36**, 495 (2013).
37. A. Nyman, M. Behm, and G. Lindbergh, *Electrochim. Acta*, **53**, 6356 (2008).
38. V. Srinivasan and J. Newman, *J. Electrochem. Soc.*, **151**, A1530 (2004).
39. K. E. Thomas and J. Newman, *J. Power Sources*, **119–121**, 844 (2003).
40. V. V Viswanathan, D. Choi, D. Wang, W. Xu, S. Towne, R. E. Williford, J.-G. Zhang, J. Liu, and Z. Yang, *J. Power Sources*, **195**, 3720 (2010).
41. Elektrische Straßenfahrzeuge - Batteriesysteme - Abmessungen Für Lithium-Ionen-Zellen, DIN SPEC 91252: 2011-01, 2011.
42. P. M. Gomadam, R. E. White, and J. W. Weidner, *J. Electrochem. Soc.*, **150**, A1339 (2003).
43. J. Cannarella and C. B. Arnold, *J. Power Sources*, **245**, 745 (2014).
44. J. Vetter, P. Novák, M. R. Wagner, C. Veit, K. C. Möller, J. O. Besenhard, M. Winter, M. Wohlfahrt-Mehrens, C. Vogler, and a. Hammouche, *J. Power Sources*, **147**, 269 (2005).
45. M. Klett, R. Eriksson, J. Groot, P. Svens, K. Ciosek Högström, R. W. Lindström, H. Berg, T. Gustafson, G. Lindbergh, and K. Edström, *J. Power Sources*, **257**, 126 (2014).